Unlocking the Full Potential of MgAgSb by Unravelling the Interrelation of Phase Constitution and Thermoelectric Properties

Amandine Duparchy, Frederic Kreps, Eckhard Müller, and Johannes de Boor**

A thorough understanding and optimization of microstructure are key for enhancing performance in thermoelectric materials. By combining high-resolution microstructural analysis with bulk transport characterization and spatially resolved Seebeck microprobe measurements, the interrelation between phase constitution and thermoelectric properties of MgAgSb, a promising p-type room temperature material is established. This study analyzes 35 MgAgSb samples with varying compositions and synthesis conditions. Scanning transmission electron microscopy with energy-dispersive X-ray spectroscopy and selected area electron diffraction reveals that remnants of constituent elements from the initial synthesis step can cause the formation of detrimental secondary phases, including a previously unnoticed, highly dispersed Ag_3Sb nanophase uniformly distributed throughout the samples. Analysis of the temperature dependence of the weighted mobility reveals differences in carrier scattering as the main reason for the different thermoelectric performance. Furthermore, a statistical analysis of weighted mobility and material quality factor versus type and amount of secondary phase reveals the secondary phases to predominantly affect the electronic (not thermal) transport, ranks them according to impact and further distinguishes classical mixing from grain boundary effects. This approach is crucial for understanding how specific phases affect material performance, identifying Mg_3Sb_2 and (Ag) as the most detrimental, but also providing guidelines for further material improvement.

1. Introduction

As society becomes increasingly concerned with sustainability and minimizing environmental impact, the demand for sustainable energy systems to decelerate climate change has become critical. Traditional energy systems rely heavily on fossil fuels-based technologies[1] which not only contribute to environmental degradation but also lose significant amounts of primary energy as waste heat.[2] In this context, thermoelectric materials emerge as a promising technology, converting (waste) heat directly into usable electrical energy, unlocking a potential new source of clean energy.[3,4] On the other hand, thermoelectric devices can also employ the Peltier effect for silent and rapidly adjustable solid-state thermal management. Thermoelectric power generation has already found applications in a variety of fields, from corrosion protection at pipelines to wearable medical devices and aerospace industry, while Peltier technology is an integral part in many medical and opto-electronic devices as well as a promising approach for thermal management in electrical vehicles.[5–9] The performance of TE materials is characterized by the figure of merit $zT = S^2 \sigma T/\kappa$, where S is the Seebeck coefficient, σ the electrical conductivity, T the absolute temperature and κ the thermal conductivity.[10]

During recent years p-type MgAgSb has attracted a lot of attention due to its high thermoelectric performance between 300 and 573 K.[11–13] This material system fills a gap in the p-type material spectrum, bridging the performance between the low temperature Bi_2Te_3-based solid solutions and mid-temperature materials such as Skutterudites,[14] SnSe,[15] or PbTe.[16] Te-based TE materials are not suitable for large-scale applications because tellurium is an extremely rare element (with a fraction of ≈0.001 ppm in the Earth's crust[17]) and accessible as a byproduct from Cu mining. With increasing amounts of Cu recycled, Te will be produced less, making its price even more volatile. On the other hand, MgAgSb is composed of less scarce and better available elements making it a viable option for large-scale applications. Additionally, MgAgSb has demonstrated device maturity, particularly when paired with n-type Mg_3Sb_2 or n-type Mg_2X, (X = Si, Sn, Ge) offering a competitive alternative to fully

---

A. Duparchy, F. Kreps, E. Müller, J. de Boor
Institute of Frontier Materials on Earth and in Space
German Aerospace Center (DLR)
D–51170 Cologne, Germany
E-mail: amandine.duparchy@dlr.de; johannes.deboor@dlr.de

E. Müller
Institute of Inorganic and Analytical Chemistry
Justus Liebig University Giessen
Heinrich-Buff-Ring 17, D–35392 Giessen, Germany

J. de Boor
University of Duisburg-Essen
Faculty of Engineering
Institute of Technology for Nanostructures (NST) and CENIDE
47057 Duisburg, Germany

The ORCID identification number(s) for the author(s) of this article can be found under https://doi.org/10.1002/adfm.202510200

DOI: 10.1002/adfm.202510200

Table 1. Nominal sample compositions, involvement of the cleaning step and expected secondary phases according to the measured effective composition of selected samples. (Ag) stands for Ag-rich solid solution.

Sample name	Nominal composition	Cleaning step	Expected secondary phases
c-8-7	$MgAg_{0.97}Sb_{0.995}$	Yes	Sb
nc-8-3	$MgAg_{0.97}Sb_{0.995}$	No	Mg_3Sb_2 + (Ag)
c-8-14	$MgAg_{0.94}Sb_{1.03}$	Yes	Mg_3Sb_2 + Sb
c-8-16	$MgAg_{0.915}Sb_{0.901}$	Yes	Mg_3Sb_2 + (Ag)

Bi_2Te_3-based thermoelectric modules.[18–21]

The efficiency of thermoelectric materials is not only determined by their main chemical composition and dopants but is also influenced by microstructural features. Among these, secondary phase inclusions and grain boundaries play significant roles and their effects can be either functionally beneficial or detrimental depending on their nature and distribution. Within a classical effective medium model, secondary phases reduce the thermoelectric performance of an optimized material, but features like energy-selective carrier scattering[22] or topologically protected transport can overcome this limit.[23,24] Furthermore, both interfaces linked to secondary phases and grain boundaries can act as scattering centers for phonons, thereby reducing the material's thermal conductivity, improving the TE figure of merit if not strongly scattering the charge carriers as well, and thus, significantly reducing the electrical conductivity.

An effective synthesis route was initially developed by Zhao et al.[12] and further refined by Rodriguez-Barber et al.[25] This method consists of two steps: ball milling and annealing of the MgAg precursor, followed by a second ball milling step of MgAg and Sb and a final sintering step to form MgAgSb. However, MgAgSb exhibits a phase transition from the high-performance alpha phase to the metallic beta phase at ≈300 °C and the semiconducting, but inferior gamma phase at ≈350 °C. Thus, to avoid the detrimental phase transition the compaction/annealing temperature of MgAgSb should be kept below 300 °C. However, this implies limited diffusivities of the involved elements and hence achieving a fully reacted, homogeneous material distribution remains a significant challenge. Hence, despite the synthesis route of MgAgSb being in principle well-established, experimental results show that MgAgSb is a very sensitive material, highly susceptible to minimal changes in process parameters. Several works on MgAgSb report strongly varying average figure of merit when using the same nominal composition ($MgAg_{0.97}Sb_{0.995}$) and a similar synthesis route which consist of two steps of high energy ball milling (Mg together with Ag first and then MgAg together with Sb), followed by an annealing under uniaxial pressure. The average zT in the temperature range from room temperature to 573 K varies from $zT_{avg} = 0.77$[25] through 0.9[18,25,26] to 1.1,[11,27] presumably depending on synthesis control. Some understanding on this was provided by Rodriguez-Barber et al.,[25] who demonstrated that adding an intermediate annealing step of MgAg as a precursor before adding Sb promotes the reaction between elemental Mg and Ag, thereby reducing the formation of Ag-rich secondary phases in the final material, resulting in an increase of zT_{avg} from 0.77 to 0.95. Later on, Duparchy et al.[27] showed that some of the constituents were adhering preferentially to the wall, thus slightly shifting the gross composition of the second ball milling step in a non-cleaned vial. To solve this, an intermediate cleaning step of the ball milling jar was introduced after the first milling step, revealing that removing excess of Mg and Ag residues from the milling jar improves the reproducibility of the synthesized samples and their performances.[27] They also showed experimentally that the single-phase region is compositionally very narrow, confirming point defect calculations by Feng et al.,[28] focusing on the role of lattice point defects (Ag vacancies, Ag on Mg site) and their effects on electronic and thermal properties. The calculations show that the formation energies for both defects (Ag_{Mg} antisite defects or Ag vacancies) are relatively similar for the different thermodynamic limits, which supports the conclusion that MgAgSb has a very narrow stable compositional range. This narrow window limits the feasible adjustment of charge carrier concentration by varying intrinsic defect densities and easily leads to the formation of secondary phase precipitates in the material if the target stoichiometry is not ideally met. Duparchy et al.[27] found a correlation between effective composition, content of secondary phases and resulting TE properties whereas the significance of the study was limited by the employed analysis methods, in particular the limited compositional and spatial resolution (microscale) of scanning electron microscopy combined with energy dispersive X-ray spectroscopy (SEM-EDS) and X-ray diffraction (XRD).

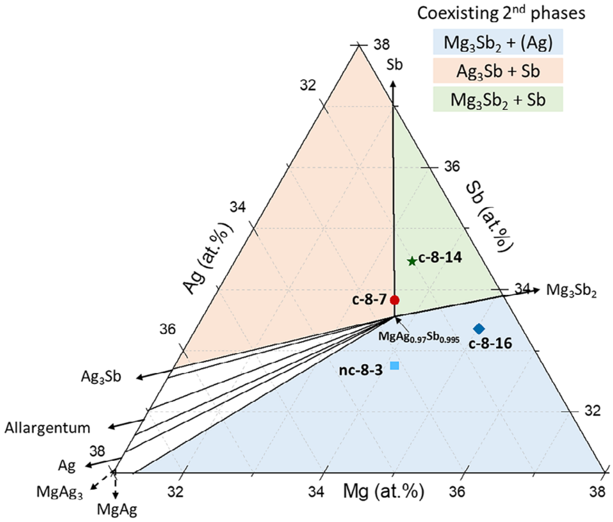

Figure 1. Central section of the Mg-Ag-Sb phase diagram at room temperature, four samples are indicated according to their measured global composition. These are nc-8-3, c-8-7 with $MgAg_{0.97}Sb_{0.995}$ as nominal composition, c-8-14 with $MgAg_{0.94}Sb_{1.03}$ nominal composition and c-8-16, nominally $MgAg_{0.91}Sb_{0.901}$. The black arrow indicates $MgAg_{0.97}Sb_{0.995}$, the assumed single-phase composition. The colored sectors in the phase diagram are different three-phase areas: MgAgSb plus two coexisting secondary phases.

The lack of high-resolution microstructural analysis for MgAgSb material prevents accurate phase identification, limiting our knowledge of phase formation mechanism, their occurrence, and their impact on the material's transport properties. A key challenge in fabricating high-performance p-type MgAgSb

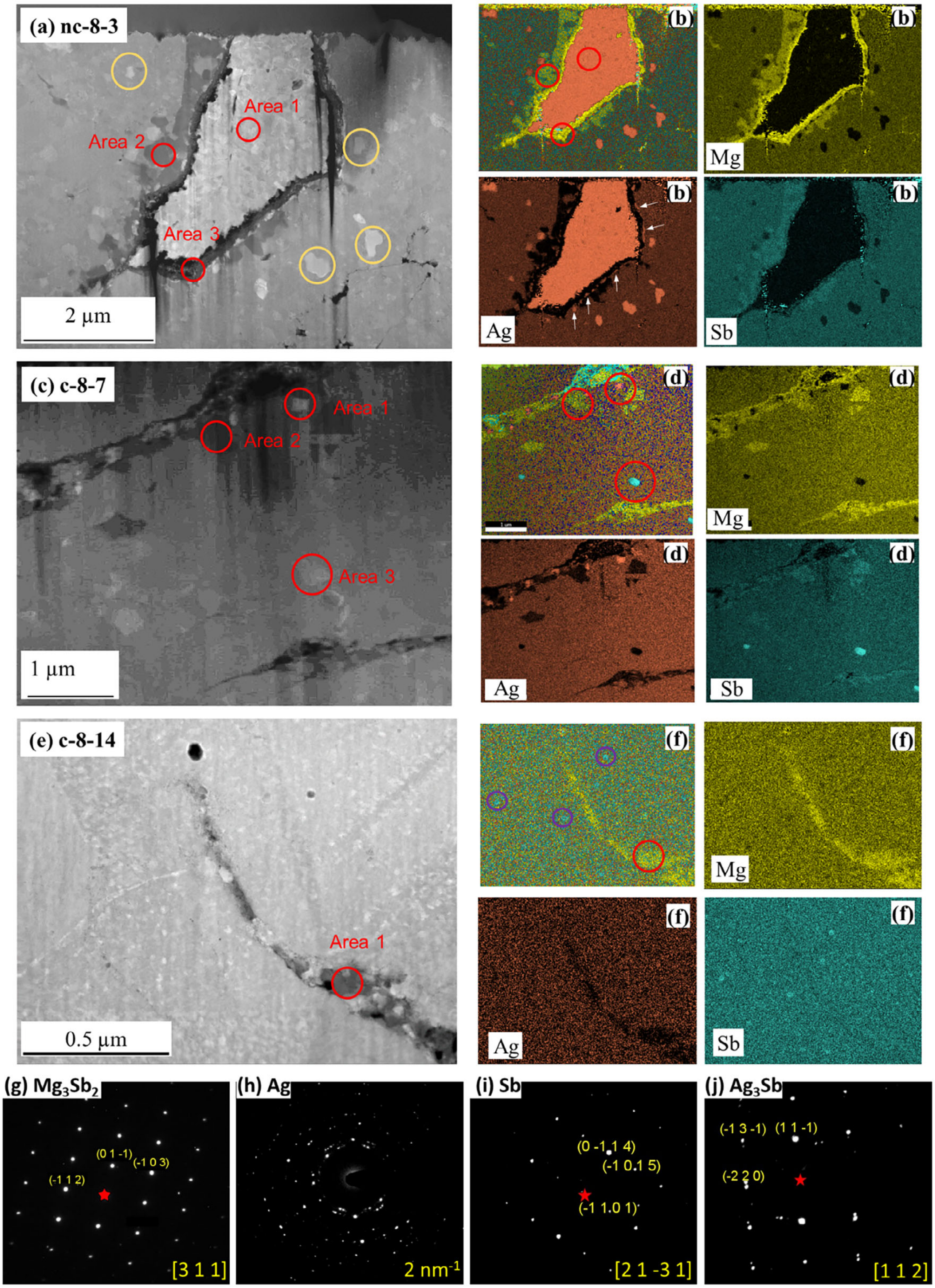

Figure 2. a) High-angle annular dark-field (HAADFSTEM image of nc-8-3 and b) the corresponding EDS element mapping; c) HAADF-STEM image of c-8-7 and d) the corresponding EDS element mapping; e) HAADF-STEM image of c-8-14 and f) the corresponding EDS element mapping. Electron diffraction pattern g) from Area 2 of nc-8-3 corresponding to Mg_3Sb_2 phase, h) of a similar area as Area 1 from nc-8-3 corresponding to Ag phase, i) of a similar area as Area 3 from c-8-7 corresponding to Sb phase and j) of a similar area as Area 1 from c-8-7 corresponding to Ag_3Sb phase. HAADF-STEM images from sample nc-8-3 and c-8-7 can be found in Figures S1 and S2 (Supporting Information) respectively.

Table 2. STEM-EDS composition results of areas 1 to 3 from nc-8-3 and c-8-7, and area 1 from c-8-14 as shown in Figure 2.

	nc-8-3			c-8-7			c-8-14
	Area 1	Area 2	Area 3	Area 1	Area 2	Area 3	Area 1
Mg (at.%)	2.7	54.8	75.2	2.3	45.8	7.8	53.8
Ag (at.%)	91.8	2.7	0	76.4	9	3	2.4
Sb (at.%)	5.5	42.5	24.8	21.3	45.2	89.1	43.8
Probable phase	(Ag)	Mg_3Sb_2	Mg_3Sb_2 + Mg	Ag_3Sb	Mg_3Sb_2	Sb	Mg_3Sb_2

material lies in its high sensitivity to minor variations in effective composition and synthesis parameters. This sensitivity to small amounts of secondary phases and compositional changes is particularly critical compared to other material systems, where secondary phases are observed but have less pronounced effect on TE properties. For example, de Boor et al.[29] observed that 4 wt.% of MgO in Mg_2Si reduces zT_{avg} by 10 to 15%, which is detrimental but not dramatic. Similarly, studies on $Mg_2(Si,Sn)$ solid solutions[30,31] have shown the formation of Si-rich islands in both n- and p-type materials. Sankhla et al.[31] demonstrated that further milling time can reduce the Si-rich phases content, though with limited improvement in the material's properties.

This work aims at investigating the interrelation of phase constitution and thermoelectric properties using combined microstructural measurements. Scanning transmission electron microscopy (STEM) with energy-dispersive X-ray spectroscopy (EDS) with higher lateral resolution than standard SEM together with Selected Area Electron Diffraction (SAED), were used to accurately identify secondary phases on both the micro- and nanoscale. P-type samples were synthesized with small differences in synthesis parameters, resulting in different effective compositions and varying amount and type of secondary phases. By detailed microstructural investigations and careful analysis of STEM images and transport properties, we identify the key reasons for the usually observed high abundance secondary phases in MgAgSb, limiting the reproducible synthesis of high performance MgAgSb. Indeed, the limited resolution of MgAgSb microstructural analysis prevented to distinguish between two possible explanations for the secondary phases' formation: that they are a consequence of the overall off-stoichiometry of the samples, or that they included meta-stable phases indicating insufficient homogenization. We furthermore quantify the impact of different secondary phases, identifying the most detrimental ones and derive suggestions how to improve material performance. Beyond quantifying phase impacts, this statistical approach also provides a way to possibly detect concentration-independent effects, such as complexions or point-defect structures.

2. Results

Four samples were selected for the in-depth microstructural analysis. These samples were chosen to represent different synthesis routes (with / without cleaning step) and varied compositions, as detailed in **Table 1**. Duparchy et al.[27] previously conducted a comprehensive microstructural analysis using two methods – SEM-EDS and XRD, however, these methods did not always lead to consistent results.[27] Here we enter new territory by focusing on one sample from each region of the ternary phase diagram as shown in **Figure 1** (containing in principle Mg_3Sb_2 + (Ag), Ag_3Sb + Sb and Mg_3Sb_2 + Sb as secondary phases coexisting with the MgAgSb homogeneous matrix), employing STEM-EDS and SAED for an unambiguous phase identification and a characterization of the phase constitution on micrometer and nanometer scale.

Figure 2, in combination with **Table 2**, shows that the first three samples contain different secondary phases. The last sample, c-8-16, was used for consistency check. In this study we will focus on secondary phases in the material. However, it is important to note that the majority of the material consists of a uniform phase – the MgAgSb matrix. In sample nc-8-3, three distinct secondary phases are observed, exemplarily indicated by circles labeled as Area 1, 2, and 3 in Figure 2a. Elemental mapping combined with point identification analysis revealed that Area 1, a relatively large inclusion of almost 5 µm in size, is a silver-rich phase, potentially allargentum ($Ag_{1-x}Sb_x$, $0.08 < x < 0.18$) or elemental silver with dissolved Sb and Mg. Areas 2 and 3 are rich in Mg and Sb, with different ratios, likely containing the Mg_3Sb_2 phase. Area 3 exhibits a 75:25 ratio of Mg and Sb, considerably higher in Mg content than the one required to form Mg_3Sb_2 single phase, while Area 2 is relatively close to the expected composition (60:40 ratio). Such large deviations in Mg and Sb content in Area 3 from the Mg_3Sb_2 composition cannot be attributed to a measuring artifact or the overlap of the excitation area with another neighboring phase and rather indicate that Area 3 comprises more than a single phase, possibly a fine scaled composite of Mg_3Sb_2 and Mg occurring in separate domains. Hence, what we see is Mg-Mg_3Sb_2 nano-composite surrounding the Ag-rich inclusion which itself is surrounded (although not completely) by Mg_3Sb_2 phase close to stoichiometry. Thus we observe the reactants for MgAgSb unreacted even though they are situated in close vicinity. It is striking that the large Ag particle is surrounded by an Ag-free belt whereas this belt is neighbored by Ag-rich islands also at its outside (indicated by white arrows in Figure 2b). Looking carefully at the phases in the matrix, one can notice that there is another Ag-rich phase (yellow circles in Figure 2a) that looks different compared to Area 1. These Ag-rich islands enclosed in the MgAgSb matrix visible in Figure 2b doesn't show any Mg_3Sb_2 margin. Due to the shape, grain structure and the small size of those phase domains, another formation genesis is assumed for them, different from that of Area 1, probably having precipitated from the matrix.

Sample c-8-7 also contains three distinct secondary phases (Area 1, 2, and 3; Figure 2c,d). In this case, Area 1 is Ag-rich with

Table 3. Measured d-spacings (Å) of some regions of nc-8-3 and c-8-7 compared to literature d-spacings of cubic Ag, allargentum, trigonal Mg_3Sb_2, dyscrasite and trigonal Sb respectively. Composition, crystal system, space group and the lattice parameters of each phases are given in Table S3 (Supporting Information).

nc-8-3			c-8-7	
Area 1			Area 1	
Measured	Cubic Ag[32]	$Ag_{1-x}Sb_x$[32]	*Measured*	Ag_3Sb[33]
2.364	2.359	2.548	2.69	2.61
2.054	2.044	2.370	2.44	2.42
1.453	1.445	2.252	2.38	2.29
1.239	1.231	1.756	1.91	1.71

Phase similar to Area 2		Phase similar to Area 3	
Measured	Trigonal Mg_3Sb_2[34]	*Measured*	Trigonal Sb[35]
3.942	3.960	3.58	3.54
3.789	3.614	2.26	2.25
3.458	3.473	1.96	1.93
3.413	3.473	1.88	1.88
/	2.670		
2.369	2.410		

some Sb, likely Ag_3Sb following the 75:25 ratio. Area 2 is Mg- and Sb-rich, similar to Area 2 of nc-8-3, and is probably Mg_3Sb_2. Area 3 is Sb-rich.

Finally, in sample c-8-14, elemental mapping identified two secondary phases. The composition was measured by EDS of Area 1 only (red circle; Figure 2e,f) and corresponds to the Mg and Sb-rich phase which was also found in sample c-8-7 and nc-8-3. The second side phase indicated by purple circles is too small to be reliably analyzed but can be identified as an Sb-rich phase. As there is no Sb-rich phase other than Sb, the small dots are probably Sb. Importantly, this cannot be Ag_3Sb as it should be visible in the Ag signal otherwise.

To accurately identify the phases in each sample, SAED diffraction was performed on samples nc-8-3 and c-8-7. The *d*-spacings are given in **Table 3** while the Scherrer (ring) and single crystal SAED diffraction patterns of some regions of nc-8-3 and c-8-7 are shown in Figure 2g–j and can be found in more detail in Figures S2 and S3 (Supporting Information). SAED diffraction analysis of a spot like Area 1 in sample nc-8-3 revealed that the *d*-spacings of this phase match those of cubic silver, ruling out the allargentum phase (Table 3). This silver particle is relatively large (≈5 µm) meaning that it probably is unreacted silver, remaining from the uncleaned jar walls. This is an indication that the cleaning step is very important to synthesize a material as phase-pure as possible. SAED diffraction was also performed on a similar area as Area 2 from sample nc-8-3 confirming that this phase is trigonal Mg_3Sb_2. When analyzing the *d*-spacings of Mg_3Sb_2, one specific *d*-spacing appears twice in the literature (3.473 Å). This duplication arises from the material's crystallographic symmetry, as certain orientations can yield equivalent *d*-spacings. Our measured data aligns with the literature data: we observe two similar, though not identical values. Additionally, one *d*-spacing (2.67 Å) is absent in our measurements. This can be attributed to the nature ofSAED, where not all orientations are probed during tilting. However, all other *d*-spacings match the expected values, confirming the reliability of our results. In sample c-8-7, Area 1 was identified as dyscrasite (Ag_3Sb), while Area 3 was determined to be trigonal Sb, a phase also found in sample c-8-14.

In **Figure 3**, the XRD patterns of the four samples analyzed by STEM and SAED are given, together with the identified secondary phases and Rietveld refinement data in **Table 4**. The phases identified by XRD are the same as those identified by STEM and SAED, confirming the characterization. The obtained R-factors are acceptable values for a standard XRD and a multiphase sample. Also, the Rwp is somewhat similar for all samples changes smaller than 15%. The Goodness of fit varies a bit more but is still acceptable for all samples. The obtained R-factors are acceptable for a standard XRD and multiphase samples. The Rietveld refinement weighted fractions and R-factors of all other samples can be found in the Supporting Information.

Further analysis was conducted on nc-8-3 and c-8-7 samples, both with a nominal composition of $MgAg_{0.97}Sb_{0.995}$, to examine the phase constitution and morphology at the nanoscale. **Figure 4** shows STEM-EDS elemental mapping from MgAgSb matrix regions of both samples at high magnification, allowing comparison of their micro- and nanostructure (low magnification images can be found in Figure 2). The only processing difference between the two samples is the addition of an intermediate cleaning step of the jar before adding Sb powder to the pre-reacted MgAg precursor. At the microscale, i.e., imaged at low magnification, both samples appear similar, with the main phase, MgAgSb, apparently homogeneous. However, at the nanoscale, c-8-7 appears homogeneous, while the nc-8-3 matrix is clearly inhomogeneous, displaying a negative correlation between Mg and Ag (and a relatively homogeneous Sb content). Thus, one could conclude that the nanophase uniformly forms in the samples synthesized without intermediate cleaning step. Another EDS mapping was performed on sample nc-20-12 (Figure S3, Supporting

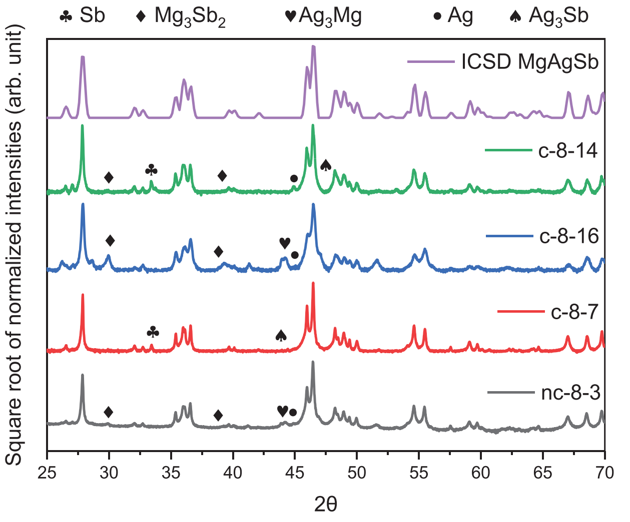

Figure 3. X-ray diffraction patterns of MgAgSb single phase (ICSD) as well as samples c-8-14, c-8-16, c-8-7 and nc-8-3.

Table 4. Phase fractions determined by Rietveld refinement in weight percent, as well as the R-factors (R_{Bragg}, R_{wp} and goodness of fit GOF).

Sample Name	Phase amount (wt.%) [R_{bragg}]						Rwp	GOF
	MgAgSb	Mg_3Sb_2	Ag_3Sb	Ag	Sb	Ag_3Mg		
c-8-7	97.8 [6.5]	–	1.3 [2.7]	–	0.9 [5.5]	–	14.79	5.60
nc-8-3	97.0 [6.2]	1.1 [5.0]	–	1.4 [3.2]	–	0.5 [2.6]	12.66	4.84
c-8-14	97.3 [3.3]	0.5 [3.3]	–	0.2 [2.5]	2.2 [3.6]	–	12.20	2.12
c-8-16	89.1 [2.9]	3.1 [3.2]	–	2.0 [2.9]	–	5.8 [2.6]	13.33	1.87

Information) which is compared with sample nc-8-3 and confirms the formation of Ag_3Sb nanophase when the sample is synthesized without cleaning step.

Sample c-8-7, synthesized with cleaning step, is located in the upper left sector of the ternary diagram (Ag_3Sb + Sb region), see Figure 1, while nc-8-3 appears in the lower sector of the ternary diagram (Mg_3Sb_2 + (Ag) region). Besides the cleaning step, an essential difference between the two compared samples is their position in the phase diagram, which might also be the reason for the occurrence of the Ag-rich nanophase. To test the hypothesis that the nanophase forms only in samples synthesized without cleaning step, a new sample (c-8-16) with a different nominal composition ($MgAg_{0.915}Sb_{0.901}$) was synthesized with cleaning step. This composition was chosen to ensure that it falls in the lower part of the ternary diagram (Mg_3Sb_2 + (Ag) region) as for nc-8-3, allowing for an evaluation whether the nanophase formation is linked to the absence of the cleaning step or mainly to a composition in the lower three-phase-sector of the phase diagram. As shown in Figure 1, the sample appears in the intended region but is slightly shifted toward Mg-rich composition, compared to nc-8-3. As shown in Figure S4 (Supporting Information), the c-8-16 sample is homogeneous with no visible Ag-rich phase at the nanoscale.

To accurately identify the Ag-rich nanophase, SAED was performed. Since the phase domains are relatively small, Scherrer diffraction was used over the matrix. The ring diffraction pattern (**Figure** 5e) was used to calculate the *d*-spacings, which are given in **Table** 5. The main intensities correspond to α-MgAgSb. However, weaker reflexes are detectable apart from the main rings. The *d*-spacings of some of these (red circles in Figure 5e) match with the literature values for *d*-spacings of orthorhombic Ag_3Sb, identifying the nanophase is dyscrasite. Note that the observation of Ag_3Sb secondary phases is not in contradiction to the Mg and Ag rich global composition of the sample as we also observed Mg_3Sb_2 and (Ag) for that sample; the finding rather points out an incomplete homogenization of the sample.

Figure 6a displays the Seebeck coefficient mapping of sample c-8-16 obtained using the Potential Seebeck Microprobe (PSM), along with a zoomed-in section (delimited by the black rectangle in Figure 6a), measured by the Transient Seebeck Microprobe (TPSM), as shown in Figure 6b. The Seebeck coefficient map reveals that the material exhibits p-type conductivity. A

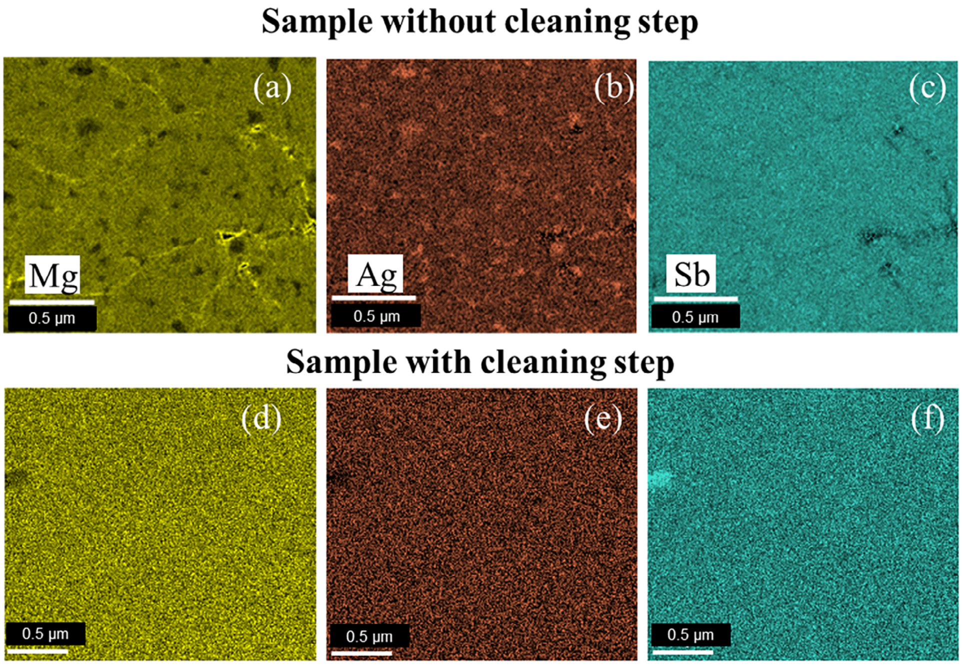

Figure 4. HAADF-STEM-EDS mapping of nc-8-3 a to c) and c-8-7 d to f) at high magnification.

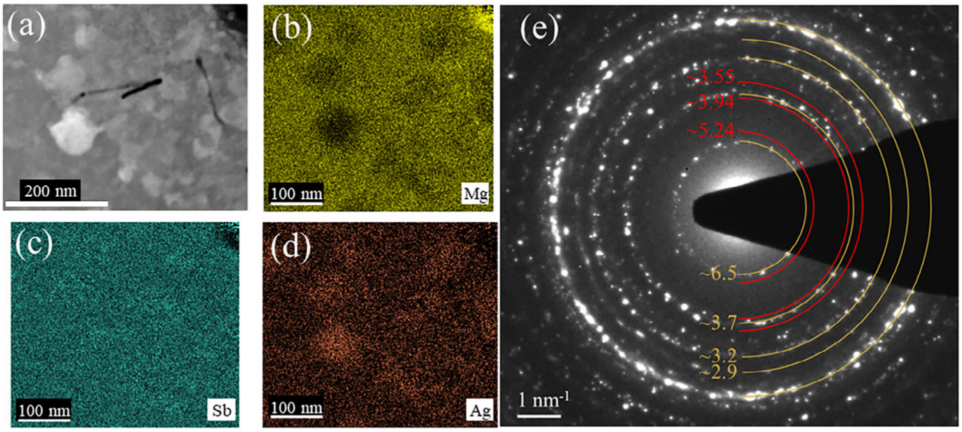

Figure 5. a) HAADF-STEM image of the MgAgSb matrix containing the nanophase and b–d) EDS elemental mapping of the nc-8-3 sample. e) shows the ring diffraction pattern of nc-8-3 with the corresponding d-spacings of MgAgSb (yellow) and the nanophase (red).

comparison between the PSM and TPSM measurements, which differ in local resolution (20–50[36] and 3–5 µm,[37] respectively), clearly shows that at a large scale, the Seebeck coefficient appears more homogeneous, with an average matrix value of 178 µV K^{-1}. In contrast, the TPSM data (Figure 6b) show stronger small-scale inhomogeneities in the Seebeck coefficient, which range in magnitude from 140 to 230 µV K^{-1}, with a matrix value of 210 µV K^{-1}. Comparing PSM and TPSM (matrix) data for the indicated black rectangle we observe differences in the average values of the Seebeck coefficient: 200 µV K^{-1} for TPSM (estimated from Figure 6d) and 180 µV K^{-1} for PSM (estimated from Figure S5d, Supporting Information), where the matrix in Figure 6d has a larger Seebeck value than the mean of Figure S5d (Supporting Information). These differences could indicate a different extent of the cold finger effect[38] due to a different tip design. On the other hand, it could also be due to an averaging of regions with large Seebeck coefficient (MgAgSb matrix) and more metallic secondary phases in the PSM due to the lower resolution, visualizing the detrimental impact of secondary phases on the bulk Seebeck coefficient of MgAgSb samples.

Figure 6c shows the BSE-SEM image of the TPSM scan area, corresponding to the area indicated by the pink rectangle in 5b, while Figure 6d presents an overlap of the TPSM scan and the BSE-SEM image. Looking at the overlay of TPSM with SEM, one recognizes a correlation between secondary phases, identified as Ag-rich phase, and low Seebeck coefficient. In particular all secondary phase domains except one are located in areas where S is <210 µV K^{-1}, and areas where the Seebeck coefficient is below 185 µV K^{-1} consistently feature at least one bright particle, i.e., a secondary phase. Exception from that rule of correlation of phase domains visible by SEM to the TPSM data can be related to different information depth of the two methods: TPSM ≈5 µm compared to 1 µm for the SEM. When interpreting the TPSM measurement values near the secondary phase regions one needs to take into account that those are usually smaller than the spatial resolution of the TPSM, hence the measurement result mostly corresponds to a weighted average of the Seebeck coefficient of secondary phase and surrounding matrix, not only laterally but also in depth. Given the significant contrast and the small size of the phase domains, it is possible that the low magnitude regions in the TPSM map represent areas where the Seebeck coefficient approaches low values or becomes negative, the former an indication of a metallic phase, the latter expected for a semiconducting n-type phase, e.g. Mg_3Sb_2. This observation aligns with the SEM-EDS measurement of the large white phases which correspond to regions enriched with silver (see Figures S6 and S7, Supporting Information). This suggests that while the PSM provides more uniform data across a large area, the inhomogeneities detected by the TPSM are not due to local variations in charge carrier concentration but rather to the morphology of the local distribution of secondary phases within the material, indicating a composite structure.

Table 5. Measured d-spacing of nc-8-3 compared to MgAgSb and dyscrasite (Ag_3Sb) d-spacing from literature.

d-spacing main phase [Å]	α-MgAgSb[13] [Å]	d-spacing reflexes [Å]	Ag_3Sb[33] [Å]
6.431	6.488	5.24	5.240
4.406	4.537	3.94	3.943
3.736	3.718	3.70	3.769
3.241	3.244	3.55	3.559
2.869	2.888		3.059

3. Discussion

This study thoroughly analyzes one sample from each out of the three main three-phase regions adjacent to the homogeneous "MgAgSb" phase of the Mg-Ag-Sb phase diagram regarding secondary phase constitution using STEM-EDS and SAED diffraction enabling reliable phase identification for the very first time. In fact, the already published studies only used STEM to study the structural details of grains[12,39] or SEM-EDS and XRD for phase identification.[25–27,40,41] Such microstructural analysis is not accurate enough to be able to differentiate secondary phases. Looking at the literature, all kind of secondary phases were identified: Ag,[27] Mg_3Sb_2,[26,27] Ag_3Sb,[25,27,42–44] Allargentum,[27] Ag_3Mg,[26] MgAg[26,27] and Sb.[25,27,42–45] Mg_3Sb_2, Ag_3Mg, Sb and Ag_3Sb are easily identified by SEM-EDS and XRD (when occurring in large

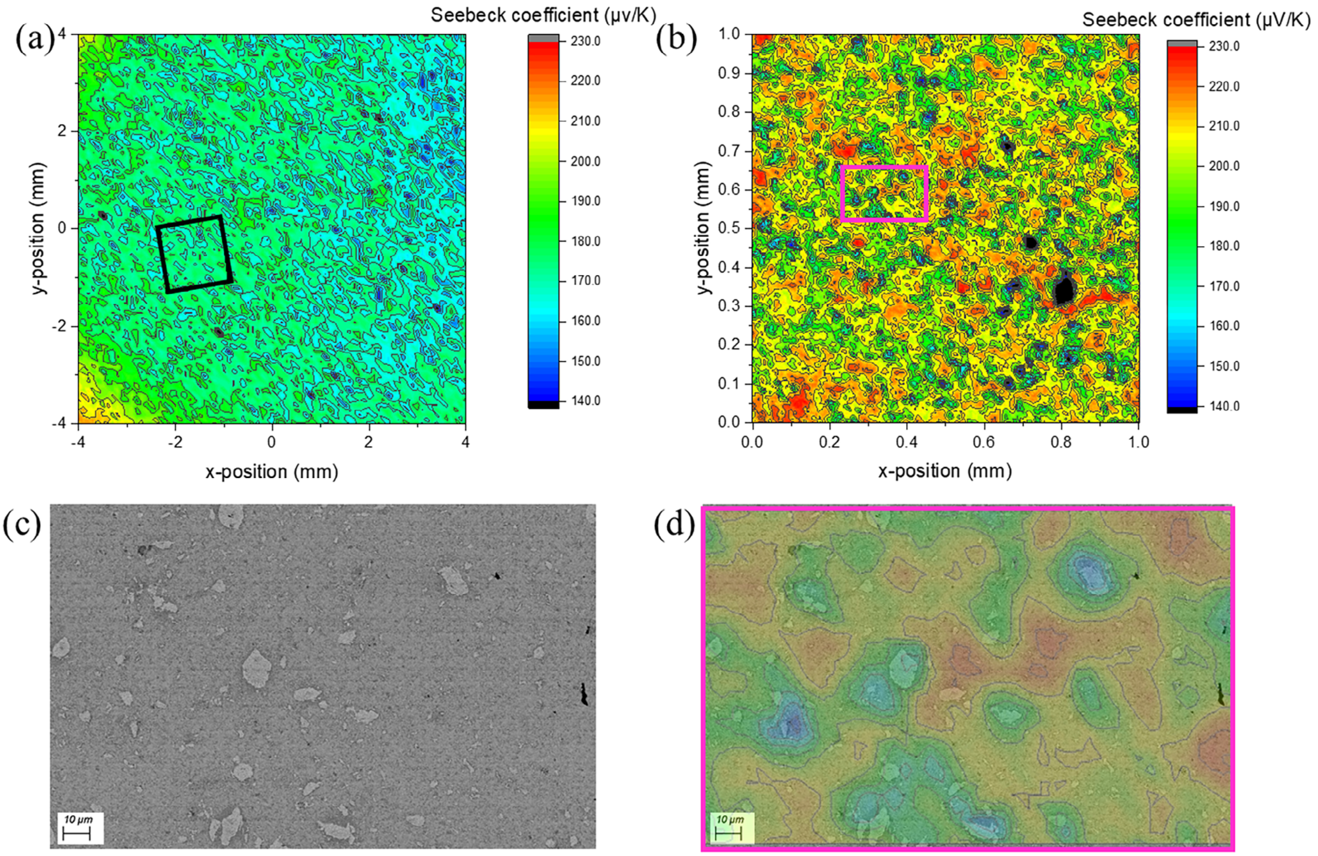

Figure 6. Seebeck coefficient map of the c-8-16 sample a) measured by PSM, b) TPSM measurement from the black frame in (a), c) backscattered electron (BSE)-SEM image of the zoom-in section and d) overlay of SEM and zoomed TPSM data (both taken from the pink rectangle in (b)).

amounts) and where confirmed by our STEM-EDS combined with SAED analysis. However, regarding Allargentum, Ag and MgAg phases, SEM-EDS combined with XRD is not sensitive enough.

First of all, Ag-rich phases can be identified as allargentum or (Ag) due to the low amount of Sb detected with EDS. In fact, according to the phase diagram developed by Okamoto et al.,[46] up to 5% antimony can be dissolved in cubic Ag, leading to a composition that SEM-EDS might misidentify as allargentum, as done in[27]. To clarify this, STEM-EDS and SAED diffraction was performed on nc-8-3 sample which contains this Ag-rich-Sb-poor phase, as shown in Tables 3 and 4. STEM-EDS revealed an Ag-rich phase with a low amount of Sb, and SAED diffraction confirmed that this phase is actually cubic Ag with some dissolved Sb, not allargentum. Furthermore, Duparchy et al.[27] detected MgAg phase by XRD while it was not confirmed by their SEM-EDS analysis, raising concerns about the reliability of the measurement. On the contrary, Camut et al.[26] did not identify MgAg by XRD but detected it by SEM-EDS. This discrepancy highlights inconsistencies in phase identification. According to the ternary phase diagram, MgAgSb and MgAg do not coexist, suggesting that MgAg may persist as a remnant from the second milling step of the synthesis process, reflecting a non-equilibrium state. Camut et al.[26] used a synthesis route differing slightly from that of Duparchy et al.,[27] involving the ball milling of MgAg followed by the addition of Sb without intermediate annealing under axial pressure of MgAg. This process plausibly leaves residual MgAg from the initial ball milling step, as confirmed by their SEM-EDS results. However, in Duparchy et al.'s[27] case, MgAg was neither expected nor identified by SEM-ESD. To investigate this further, we employed STEM-EDS to examine samples from various regions of the phase diagram at both micro- and nanoscale, including the grain boundaries. No MgAg was detected in any region. A detailed analysis of the XRD patterns revealed that the MgAg peaks overlap with those of cubic Ag (Figure S8, Supporting Information). This is supported by STEM and SAED characterization, which identified only cubic Ag in sample nc-8-3 for example. These findings emphasize the importance of advanced microstructural analysis to reliably determine phase composition and resolve ambiguities from using conventional characterization techniques.

The STEM-EDS analyses conducted on nc-8-3, c-8-7, c-8-14, and c-8-16 samples demonstrates that there is a non-equilibrium combination of secondary phases. For nc-8-3, specific secondary phases such as Ag_3Sb nanophase were found which is not expected in the region of the phase diagram corresponding to the global composition of the sample, further confirming the non-equilibrium state of the samples. In the upper right 3-phase-region of the phase diagram, the expected secondary phases are Mg_3Sb_2 and Sb which are the two only phases beside MgAgSb that have been detected for sample c-8-14. This sample is also a relatively good sample, therefore an indication that the homogenized samples are the better ones. Finally, regarding the upper left region of the phase diagram, sample c-8-7 located almost ideally at the MgAgSb – Sb line showed the presence of Mg_3Sb_2 + Sb and Ag_3Sb phase. As the sample is close to the border of the different regions, finding either Mg_3Sb_2 or Ag_3Sb is expected; having both again confirms incomplete homogenization. Hence, depending of the phase diagram region and cleaning step, some samples (the worst ones) are in non-equilibrium thermodynamically. The Ag_3Sb nanophase is found in all samples synthesized without cleaning step and probably influences the material properties. Such very fine-scaled phase mixture could be the consequence of a precipitation process during cooling down after annealing under axial pressure if the homogeneity range of the "parent" phase is larger at higher temperature. To explain the observed Ag_3Sb nanophase, the initial MgAg would need to be Ag-rich, indicating that Mg would have needed to remain preferentially on the wall and we should see a shift toward Ag for the samples synthesized without cleaning step which is not observed (see Figure S9, Supporting Information). Furthermore, the MgAg would need to be 3 to 5% Ag rich according to the Mg-Ag phase diagram[47] to expect precipitation upon cooling. However, the nominal composition for the initial ball milling step is $MgAg_{0.97}$ and thus Mg-rich, requiring an implausible and not observed large shift in stoichiometry of the final MgAgSb sample.

We therefore conclude that the formation of the Ag_3Sb nanophase is not due a precipitation mechanism, but rather due to the reaction of (unreacted) Ag from the first ball milling step with the Sb powder introduced in the second ball milling step. We also showed that even with the cleaning step, secondary phases form abundantly. Of course, if the global composition does not coincide with that of the MgAgSb phase, secondary phases are expected, this can in principle be addressed by fine-tuning of the global composition. The bigger and MgAgSb-specific challenge is the incomplete inhomogenization and with this the occurrence of different and larger amounts of secondary phases than expected according to the global composition. With the following analysis, we try to understand why these form in the material, which is crucial to improve and upscale the material synthesis.

The formation of MgAgSb and the secondary phases is related to the availability and diffusivity of the respective reactants, as well as the thermodynamic driving force for possibly competing reactions. For this we compare the reaction enthalpies for the intended reactions: $3MgAg + 3Sb \rightarrow 3MgAgSb$ with $\Delta H = -0.9$ eV and the reaction of the observed secondary phases $Mg_3Sb_2 + Ag_3Sb \rightarrow 3MgAgSb$ with $\Delta H = -0.3$ eV, which are obtained from the tabulated formation energies of the involved phases: ΔH_f (MgAg) $= -0.5$ eV, ΔH_f (MgAgSb) $= -0.8$ eV, ΔH_f (Mg_3Sb_2) $= -2.1$ eV and ΔH_f(Ag_3Sb) ≈ 0 eV; [48] for Ag_3Sb, calculated and experimental values differ, but all sources agree on $\Delta H_f(Ag_3Sb) < 0.1\ eV$.[48,49] The numbers indicate two important points: the formation energies for MgAgSb and Mg_3Sb_2 are both highly negative and the reactions will therefore occur spontaneously if the reactants are available. On the other hand, once Mg_3Sb_2 instead of MgAgSb has formed, e.g. due to a local deficiency of Ag, it is very stable and a reaction between Mg_3Sb_2 and Ag_3Sb is not very favorable and thus a homogenization to MgAgSb plausibly proceeds very slowly.

While MgAgSb is the most stable compound, kinetics give preference to the formation of secondary phases if intermixing of the reactants is incomplete. MgAg + Sb gives MgAgSb from the first moment on but a local over-stoichiometry of Mg will immediately cause the formation of Mg_3Sb_2. With this we can understand the formation of the different layers around the Ag particle in Figure 2a: when Sb is added in the second ball milling step, from the Mg–Ag leftover mixture from the jar, some Mg will preferentially react with Sb but the formed Mg_3Sb_2 will, due to its non-solubility, expel Ag, leading to the small Ag particles observed in Figure 2a. In general, this suggests that, under certain conditions, when mixed Mg–Ag has not fully reacted to MgAg, the elemental Ag, Mg, and Sb preferentially react to Mg_3Sb_2 and Ag rather than to MgAgSb. Indeed Rodriguez-Barber et al.[25] demonstrated that Ag remains in the MgAg precursor material during ball milling, indicating slow Ag diffusion in MgAg during annealing, probably caused by different mechanical properties of Ag and Mg, which limits the effectiveness of the ball milling. This slow incorporation of Ag can cause local Mg–Ag excess in the second ball milling step for syntheses with and without cleaning step. Additionally, MgAg is not a line phase but has a considerable width, thus also compositional fluctuations within the MgAg phase can cause local Mg/Ag excess in the second ball milling step.

With this we have a second reaction chain that explains the observed Mg_3Sb_2 and Ag-rich secondary phases: whenever Sb meets a non-ideal Mg:Ag concentration (due to an incomplete reaction to MgAg or due to compositional fluctuation within the considerable width of the MgAg phase) in the second ball milling step, the reaction to Mg_3Sb_2 is preferred but leads to segregation of Ag on a size scale of the initial concentration inhomogeneity of even coarser. Such mechanism is summarized in **Figure 7**.

The combined effects of slow Ag incorporation, incomplete intermixing, Mg–Ag wide homogeneity range and high reactivity of Mg and Sb lead to the formation of Mg- and Ag-rich secondary phases in the final material. Duparchy et al.[27] emphasized the importance of a cleaning step to improve reproducibility and transport properties; however, even with such measures, secondary phases persist to occur. To mitigate these issues, complete diminution of the Ag particles during Mg–Ag milling and complete MgAg homogenization while keeping ideal 1:1 stoichiometry is essential. This is of particular relevance as the MgAgSb annealing is limited to 300 °C to prevent the formation of β- and γ-MgAgSb. Eliminating residual elemental species (Mg or Ag) that preferentially react with Sb helps to suppress the formation of competing secondary phases. This can be done also by increasing the MgAg annealing time to enhance Ag incorporation. Determining the MgAg stoichiometry after the first ball milling, to account, e.g., for the loss of volatile Mg, will also help to predict accurately how much Sb should be added to the material.

Such changes in material phase constitution and microstructure morphology directly influence the material transport properties. The microprobe measurement of the Seebeck coefficient (Figure 6) visualizes that certain secondary phases influence the bulk properties in a very pronounced way. The Seebeck coefficient map was obtained on sample c-8-16, which contains secondary phases in large amounts (11 wt.% in total). The microprobe measurement shows a strongly reduced local Seebeck coefficient for the secondary phases (Mg_3Sb_2, Ag, and Ag_3Mg in that case), rationalizing the observed suppression of the bulk Seebeck coefficient ($S = 210\ \mu V\ K^{-1}$ at room temperature for c-8-16,

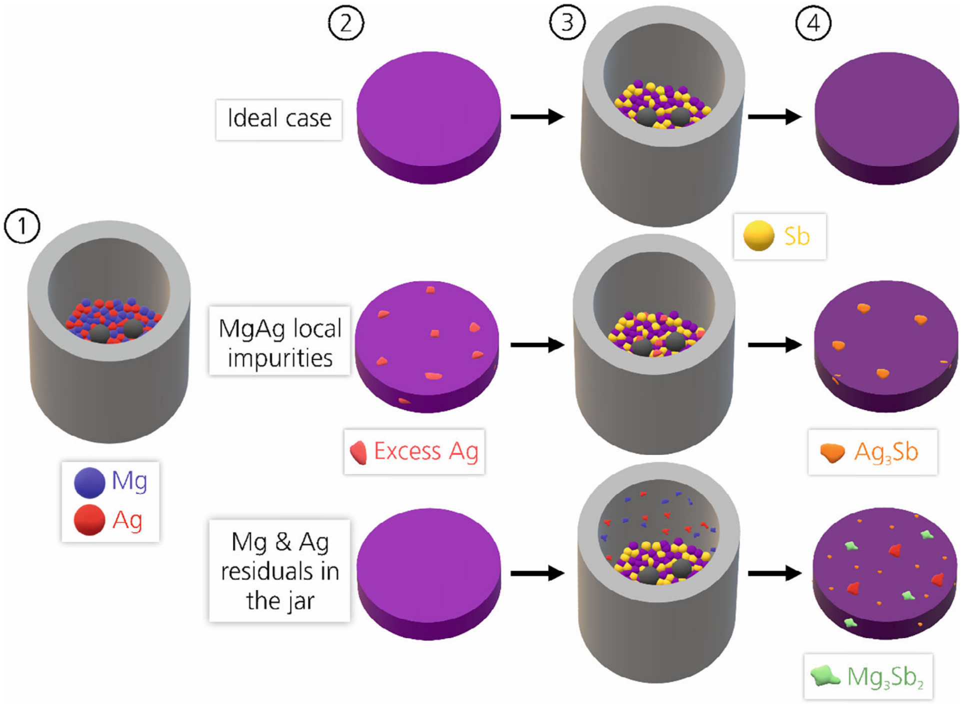

Figure 7. Synthesis and reaction scheme highlighting the mechanism of formation of secondary phases even if the global composition corresponds to single phase MgAgSb. The schematic represents four synthesis steps being: ball milling of a stoichiometric mixture of Mg with Ag, annealing under uniaxial pressure of MgAg to complete alloying, ball milling of MgAg with Sb and annealing under uniaxial pressure of MgAgSb. Three cases are shown: 1- is the ideal case when MgAg + Sb react to MgAgSb without secondary phase formation. 2- is the non-stoichiometric case with local compositional inhomogeneities in MgAg. This case covers local Ag excess at a global optimum composition. 3- is the case when there are Mg and Ag residuals from the first ball milling step in the jar.

much lower than the corresponding value $S = 250\ \mu V\ K^{-1}$ of, e.g., sample c-8-7). As shown in **Figure** 8a, the weighted mobility (μ_w) is reduced by 35% at room temperature for nc-8-3 compared to c-8-7. The main difference between those samples lies in the synthesis route. nc-8-3 undergoes a synthesis process without any cleaning of the milling jar whereas as synthesis of c-8-7 does include the cleaning. We have shown that omitting the cleaning step leads to the formation of a homogeneously distributed Ag-rich nanophase, modifying the material microstructure. This nanophase could affect the effective weighted mobility since nanostructuring often introduces a high density of grain boundaries which can scatter the charge carriers. However, comparing sample nc-8-3 and nc-20-12, both with the Ag_3Sb nanophase, we find the weighted mobilities to be different. This is attributed to the other secondary phases of the samples namely Ag_3Sb and Sb and indicates that the effect of the nanophase on the transport properties is not dominant. The prompt variation in weighted mobility for small deviations in composition (Figure 8b) is in line with the reported small variation in charge carrier density[27] and hence supports the hypothesis of a very small single-phase region for MgAgSb.

We furthermore observe differences of $\mu_w(T)$ between the samples. For c-8-7 the weighted mobility follows a $T^{-1.45}$ law, while for nc-8-3, the mobility decreases with temperature following T^{-1}. For acoustic phonon scattering, a temperature exponent between −1 and −1.5 is expected, the exact value depending on the carrier concentration, which is similar here for both samples. Hence, acoustic phonon scattering is plausibly relevant for c-8-7 and nc-8-3, but the change in the temperature dependence and the reduction for nc-8-3 suggests the influence of a further scattering mechanism. Grain boundary scattering would be a suitable candidate as it usually leads to an apparent reduction of the negative scattering exponent or even to a positive one, as, e.g., observed in Mg_2Si[50] or Mg_3Sb_2.[51]

With respect to the interpretation of the weighted mobility we need to take into account that it is introduced assuming a single-phase material, while here we are looking at composites with more or less uniformly distributed secondary phases, making the measured value an effective weighted mobility. Therefore, its variation cannot directly be ascribed to changes in the electronic band structure or carrier mobility due to, e.g., grain boundary scattering in the matrix but does also reflect the effect of secondary phases, their size, shape and local distribution. As changes in electronic band structure of the MgAgSb matrix phase are not plausible as band structure is mainly bound to composition, the observed reduction in weighted mobility and change in its temperature dependence should be interpreted as mixing of MgAgSb with dispersed secondary phases (composite effect) or further effects like those due to grain boundary decorations or formation of grain boundary phases.

For example, a similar effect is given by Villoro et al., who developed a better understanding on how grain boundaries can influence electronic properties through their study on half-Heusler compounds.[52,53] They demonstrated that increasing the

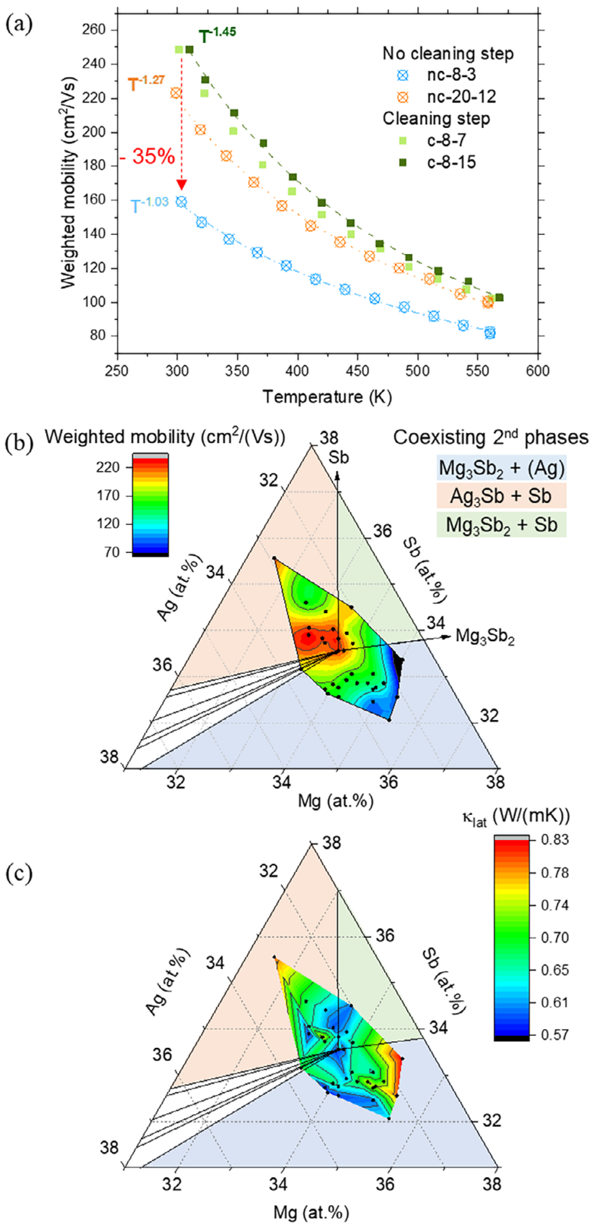

Figure 8. a) Weighted mobility of nc-8-3, nc-20-12, c-8-7 and c-8-15. Symbols represent the measured temperature dependence of samples with and without cleaning step and dashed lines represent the fitted exponential functions. b) Overlay of the central part of the ternary phase diagram and a weighted mobility map as a function of the measured global composition and c) Overlay of the central part of the ternary phase diagram and the lattice thermal conductivity as a function of the measured global composition. The colored sectors in the phase diagram are 3-phase areas: MgAgSb plus the coexisting secondary phases. Data from all 35 samples for which the statistical analysis was performed are plotted.

quantity of a grain boundary phase – also referred as grain boundary complexions, distinct 2D phases that form exclusively at grain boundaries but are not thermodynamically stable as a stand-alone 3D bulk phase – can either enhance or hinder transport properties depending on the composition and structure of these complexions. For example, Villoro et al. observed in TiCoSb half-Heusler compounds that Fe dopant segregates at the grain boundaries.[52] This segregation suppresses the electrical resistivity by reducing electron scattering.

The effect of potential complexions in off-stoichiometric MgAgSb is expected to scale with the concentration of grain boundaries and might depend on the respective three-phase-region of the phase diagram where the sample is located. As the MgAgSb grain size is ≈500 nm for all samples studied (Figure S10, Supporting Information) a strong variation of grain boundary density is not expected and can thus not explain differences between the samples. Importantly, a complexion effect is largely independent of how large the off-stoichiometry is (i.e., how far the effective composition of the sample deviated from single-phase MgAgSb) and can thus be differentiated from the composite effect of secondary phases, whose impact on the effective TE properties scales approximately linearly with the secondary phase amount. This is because complexions are extremely thin – merely a few atomic layers – and will consume only very little material to form and cover all available grain boundaries. Essentially, a complexion effect should materialize in an abrupt change in mobility when going from one region of the phase diagram to another, while a secondary phase composite effect should lead to an approximately linear decrease when going farther away from the single-phase region.

The variation of the lattice thermal conductivity (κ_{lat}) of the samples is not large, with the exception of three samples all values are within 0.65 W/(mK) +- 0.06. This clearly shows that the effect of the secondary phases is way more relevant for the electronic transport properties than for the thermal transport properties. Furthermore, given an experimental measurement uncertainty of 8% for the total thermal conductivity (κ) (and a similar one for κ_{lat}[54]) a discussion of the observed changes might lead to overinterpretation. We will therefore restrict the statistical analysis to the weighted mobility as well as the quality factor (B) and the temperature averaged figure of merit.

To further investigate the effect of the type and amount of secondary phases on the weighted mobility the material quality factor and the temperature averaged figure of merit a statistical approach is adequate due to the complexity of the influencing factors. By using a statistical analysis, we can quantify the relative importance of each secondary phase, allowing us to systematically rank their impact on the weighted mobility. To do so, the weighted mobility, quality factor and temperature averaged figure of merit of all samples was (least-square) fitted to Equation (1). All samples from this study (Table S1, Supporting Information) where included and the previously[27] erroneously identified MgAg and allargentum phases were considered as cubic Ag in this analysis, as was clarified by our study here. This means that the weight percentages of allargentum and MgAg calculated through Rietveld refinement earlier were counted as Ag content here.

The predicted mobility, quality factor and temperature averaged figure of merit according to Equation (1) shows a good agreement with the measured value plotted in **Figure 9a–c**, with $R^2 = 0.91$; 0.92, and 0.89 respectively, suggesting that the method used to determine the sensitivity parameter is adequate. As the figure of merit depends on the carrier concentration while quality factor and *weighted mobiltiy* are the more fundamental optimization parameters, we will focus the rest of the analysis on those two

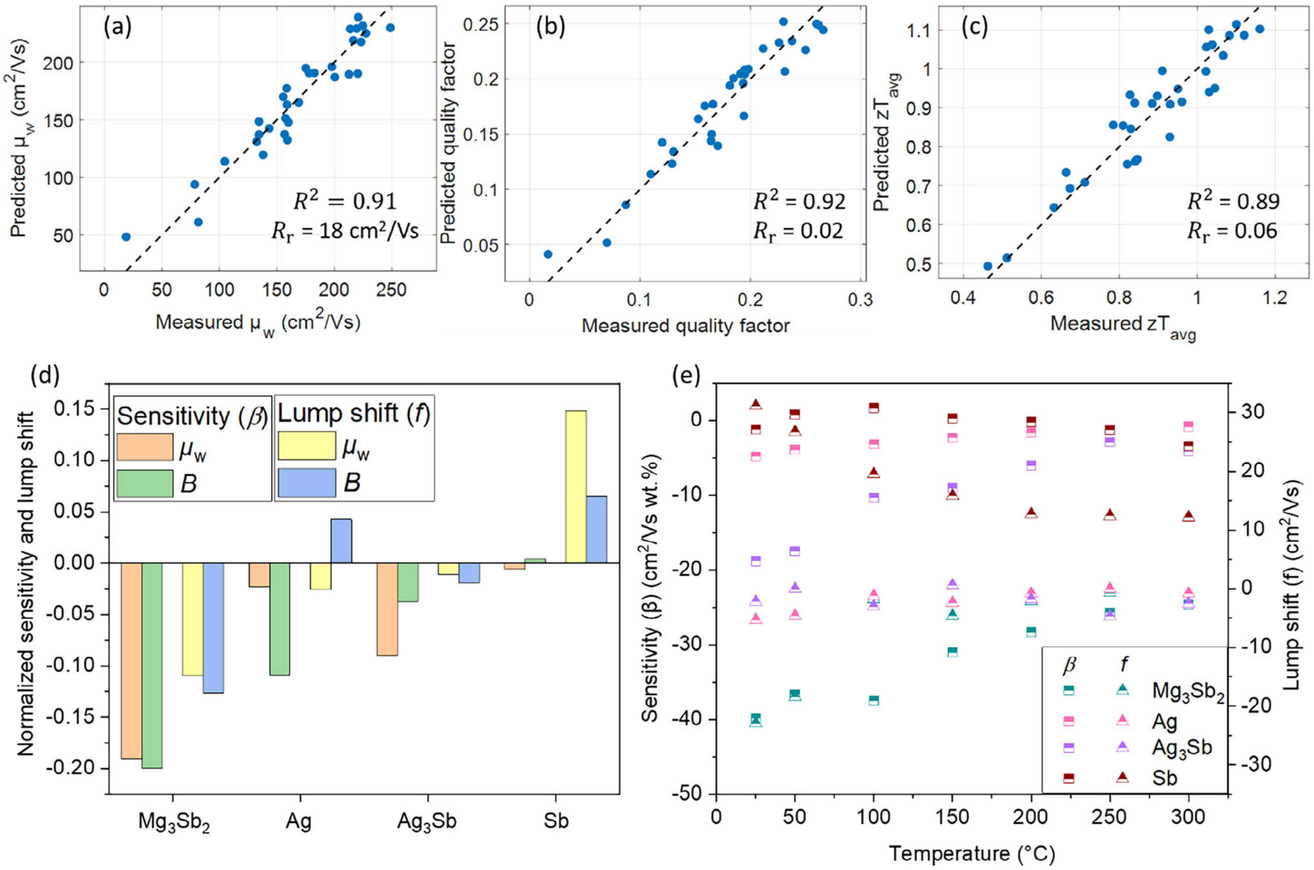

Figure 9. Measured versus least-squares fitted a) weighted mobility (μ_w), b) quality factor (B) and c) average figure of merit (zT_{avg}) on the temperature range from 25 to 290 °C; d) Normalized sensitivity (β) and lump shift (f) of the weighted mobility and quality factor with respect to phase content and type and e) sensitivity and lump shift of the weighted mobility versus temperature.

properties. Normalized sensitivity (β) and lump (f) coefficients of the weighted mobility, the quality factor and figure of merit with respect to phase content and type are given in the Figure S11 (Supporting Information).

The analysis results in large negative sensitivity parameter for Mg_3Sb_2, and, to a lesser extend Ag_3Sb and (Ag) phases respectively, for both the quality factor and the weighted mobility (Figure 9d,e), indicating (large amounts of) Mg_3Sb_2 and Ag_3Sb to be most detrimental. We observe relatively large lump shifts for Mg_3Sb_2 (negative) and Sb (positive), which is an interesting finding. These are physically motivated by possible complexion effects on the weighted mobility assuming that Mg_3Sb_2 excess leads to grain boundaries that reduce carrier mobility whereas assumingly Sb-enriched boundaries lead to a substantial enhancement of conductivity and weighted mobility, due to formation of different grain boundary decorations in dependence of the off-stoichiometry that is indicated by secondary phase constitution. Mathematically this is evidenced, e.g., by a clearly observable trend of the mobility residuals if the lump shift coefficients are omitted (f_i = 0, see Figure S12d, Supporting Information) but show only random noise when the lump shift f_i are included in the model (Figure S13d, Supporting Information)– consistent with a well-fitted model. Our analysis hence suggests occurrence of a substantial concentration-independent effect of Mg_3Sb_2 and Sb on the mobility. Alternatively, this could be due to differences in the intrinsic defect concentrations in MgAgSb when in (local) equilibrium with different secondary phases (e.g., less Ag vacancies in the Ag-rich, Sb-poor state compared to the Ag-poor, Sb-rich state[11,55]) which influences the scattering of the charge carriers. The analysis of the weighted mobility was extended from room temperature to higher temperatures to extract the temperature dependence of the sensitivity and lump parameters, providing insights into how grain boundaries influence transport. Figure 9e, shows that the reduction due to secondary phases decreases at high temperatures. This can be rationalized as scattering mechanisms other than those related to the secondary phases gain importance, most likely scattering with acoustic phonons, thereby reducing the absolute impact of secondary phases. Additionally, the temperature dependence analysis confirms that Sb has a positive effect on the mobility for all temperatures. As for samples with high Sb content no increase in the Seebeck coefficient is observed in Figure S14 (Supporting Information), the effect of Sb is presumably rather a suppression of grain scattering than energy filtering. As substantial changes in point defect configuration could otherwise explain mobility differences independent of phase concentration, the observed mobility shifts—particularly those linked to the occurrence of antimony—are more plausibly attributed to complexion effects at grain boundaries, driven by local compositional excess. The positive lump shift for Sb indicates a positive effect of small amounts of Sb as secondary phase in MgAgSb on the thermoelectric performance but we note that further interface characterization is required to prove this finding as well as the involvement of further samples to confirm the surprisingly large ratio of f_{Sb} and β_{Sb}.

Furthermore, with large negative mobility shift and sensitivity coefficients Mg_3Sb_2 is the secondary phase that causes the highest absolute change in weighted mobility suggesting that it is a thermoelectrically very detrimental secondary phase. This emphasizes that some secondary phases (Mg_3Sb_2 in our case) have a more pronounced negative effect on μ_w than others. Mg_3Sb_2 is a well-known thermoelectric material that exhibits n-type behavior when being Sb-deficient and p-type behavior when Mg-deficient. If we assume that Mg_3Sb_2 secondary phase as observed in MgAgSb follows the behavior expected from the global sample composition, this would indicate that samples from the green region in Figure 8b are expected to contain p-type Mg_3Sb_2 while samples from the blue region should contain n-type Mg_3Sb_2, where the latter should have the more detrimental effect on the effective Seebeck of the p-type MgAgSb sample. Indeed, analyzing the weighted mobility data in Figure S15c (Supporting Information), we find that the only sample appearing in the p-type Mg_3Sb_2 region of the phase diagram (c-8-14 surrounded by green) has the highest weighted mobility out of all samples. On the other hand, all the other samples appearing in the n-type Mg_3Sb_2 region (surrounded by the blue circle) show a lower weighted mobility, decreasing with an increasing amount of Mg_3Sb_2.

Regarding the impact of the highly dispersed Ag_3Sb nanophase, we have compared the two samples c-8-15 and nc-20-12. Both contain the same secondary phases and in similar quantities but one contains the nanophase and the other not (nc-20-12: Ag_3Sb (0.43 wt.%) and Sb (1.13 wt.%) versus c-8-15: Ag_3Sb (0.38 wt.%) and Sb (1.29 wt.%), respectively). According to the established model (Equation (1)) and the given coefficients, the predicted mobilities for c-8-15 and nc-20-12 are very similar (230 and 229.3 $cm^2\ Vs^{-1}$, respectively), while the experimental result is above the prediction for the sample without nanophase (249 $cm^2\ Vs^{-1}$) but below for the sample with nanophase (219.3 $cm^2\ Vs^{-1}$). Hence, for this specific example, we can estimate the impact of the Ag_3Sb nanophase to be $\approx$29 $cm^2\ Vs^{-1}$, more than 10% of the total value and hence quite significant.

Overall, through this statistical analysis, we deduce that n-type Mg_3Sb_2 is the most detrimental secondary phase type, followed by Ag_3Sb and Ag, which aligns with the assumption of Duparchy et al.[27] The latter is potentially due to the more metallic behavior combined with the tendency to form compact inclusions of Ag. The statistical analysis also indicates that excess Sb may not be critical, but a small over-stoichiometry might improve reproducibility of the fabrication process toward high performance material. The amount and type of secondary phases is thus critical for MgAgSb material.

The material's narrow phase width implies that forming a single-phase material is almost impossible. However, we can still achieve good thermoelectric properties with a low amount of secondary phases, suggesting that a narrow phase width does not necessarily hinder control over the thermoelectric material performance. In fact, a wider phase width might actually be worse, because even though this allows for single-phase formation more easily, it introduces considerable variability in the matrix's thermoelectric properties due to a variable number of charged defects. When compared to the $Mg_2(Si,Sn)$ material system,[56] MgAgSb's sensitivity is not due to its narrow phase width but rather the effect of the secondary phases, which is determined by their type and distribution with respect to the main phase. A significant difference, in that regard, between $Mg_2(Si,Sn)$ and MgAgSb is that $Mg_2(Si,Sn)$ likely undergoes a faster homogenization, with the remaining secondary phases either being insignificant (Si-rich phases) or are removed in the annealing process (Mg, Sn). In contrast, the low annealing temperature of MgAgSb, kept to avoid phase transition, might be one reason why it is technologically so challenging to get rid of the secondary phases, as it slows down diffusion. Furthermore, a small enthalpy gain by reaction of Mg_3Sb_2 with Ag_3Sb to MgAgSb means a low driving force for homogenization. From the angle of the three regions of the phase diagram, we can draw an explanation for the strong tendency to form large amounts of secondary phases. Whereas in case of Sb or Ag excess, just elemental Sb or (Ag) phase would occur (due to their low reactivity), there is, because of high reactivity of Mg, no option for the formation of a really Mg-rich secondary phase. A Mg-rich sample would, following a vectoral rule, need considerable amounts or coexisting Mg_3Sb_2 and Ag-rich phase to cover even a small Mg excess. Local fluctuations in composition which occur during synthesis would cause such a situation of Mg enrichment locally (non-reacted elemental Mg in the material residues of the non-cleaned vial). Hence, local Mg over-stoichiometry is more detrimental than that of other elements, leading to a larger fraction of secondary phases which explains why MgAgSb is such a challenging material to synthesize without secondary phases. A last point making MgAgSb difficult is that the material system has no functionally harmless secondary phases. Either we have n-type high performance TE material (Mg_3Sb_2) or metallic phases (Ag) which are both strongly reducing the Seebeck coefficient, whereas an (almost) insulting or p-type TE inclusion would be much better tolerable. A key point toward phase-pure MgAgSb seems to carefully avoid that elemental Mg meets Sb in the synthesis as this would cause segregation effects due to a strong thermodynamic preference of Mg_3Sb_2 formation leading to locally separated secondary phases in global non-equilibrium. Another crucial point is to avoid residual elemental Ag as it will also react with Sb and form Ag_3Sb phases, whether micro or nanophase which in both cases reduces the Seebeck coefficient.

4. Conclusion

In this work, we investigate the effect of microstructure in MgAgSb samples made by a combined ball milling and annealing route, in particular its phase constitution, on its effective electronic transport properties, highlighting the challenges in achieving phase pure MgAgSb of high performance. Accurate phase identification of various samples was established, revealing that the synthesized materials are not in thermodynamic equilibrium, exhibiting significant amounts of secondary phases. Our findings show that a fine-scaled composite (Mg_3Sb_2 with Mg) forms in separate domains, alongside the presence of an Ag_3Sb nanophase in some samples. This observation suggests incomplete reaction to the target MgAgSb phase, caused by incomplete homogenization of MgAg due to a limited diffusivity of Ag in the material, further complicated by the extended homogeneity range of MgAg and requisite of low annealing temperatures. We further gave evidence that such variation in phase constitution impacts drastically the material's weighted mobility, altering both its magnitude and temperature dependence. High resolution Seebeck measurement combined with the temperature dependent behavior of the weighted mobility, suggests that these changes are driven by composite and complexion effects respectively. Finally, statistical analysis of the secondary phases' impact on the weighted mobility and material quality factor first show that the secondary phases predominantly affect the electronic transport, not the thermal, in the material and secondly that their impact can be rationalized as a classical composite effect combined with complexion effects. The study concludes that the secondary phases, particularly Mg_3Sb_2, are detrimental to the material performance, and attributes their formation to the low diffusivity of Ag and high reactivity between Mg and Sb. The statistical analysis also indicates that excess Sb may not be critical, but a small over-stoichiometry might improve reproducibility of the fabrication process toward high performance material. Overall, this work highlights the critical need for controlled synthesis strategies to optimize the material properties for advanced device applications.

5. Experimental Section

Material Synthesis: Some p-type MgAgSb samples used in this study are the same as reported by Duparchy et al.[27] and further microstructural analysis has been performed on those. Nine more samples were synthesized for confirmation of results and statistical analysis. Those samples were synthesized with different nominal compositions detailed in Table S1 (Supporting Information). The synthesis route consists of a two-step high energy ball milling process with an intermediate cleaning of the vial, after the first milling step (Mg + Ag) but before the second one (MgAg + Sb), and two annealing treatments under uniaxial pressure. Cleaning the jar is critical to control the material stoichiometry and avoid secondary phases formation due to contamination. Residual mass analysis was not performed right after ball milling to quantify the contamination before and after annealing. Instead the mass of the MgAg material after each sintering and polishing was tracked, showing a loss of ≈7% of MgAg powder. The stoichiometric amounts of Mg (turnings, Merck KGaA, >99% of purity) and Ag (powder, <45 µm, Sigma Aldrich, >99.99%) are weighted according to the composition Mg_xAg_y and loaded together into a stainless-steel jar under argon atmosphere. The mixture of the elements is then ball-milled for 8 h (by a SPEX SamplePrep 8000D). Breaks after 1 h, further 2, 2, 2, and 1 h are taken during the milling process to loosen and reintegrate the powder/flakes that stick to the jar walls. The material redistribution ensures that the milling process continues effectively and an intimate intermixing between Ag and Mg takes place. Before adding Sb to the MgAg precursor, an intermediate step consisting of an annealing under axial pressure of MgAg is carried out as Mg + Ag milling for 8 h does not result in complete mechanical alloying. Without annealing under axial pressure, secondary antimonide phases would form preferentially to MgAgSb. As shown by Rodriguez-Barber et al.,[25] 30 h of milling is needed to achieve single phase MgAg, which is time- and energy-consuming. Combining milling with an annealing under axial pressure step ensures complete reaction of the material. For that, the MgAg powder is filled into a 15 mm diameter graphite die and uniaxially hot pressed (in a Dr. Fritsch DSP510 direct sinter press) for 8 min at 673 K under 85 MPa. The obtained Mg_xAg_y pellet is crushed in the high energy ball mill for 18 min before adding the Sb (crushed granules, 3–15 mm, Sindlhauser Materials GmbH, 99.999%) according to the stoichiometry $Mg_xAg_ySb_z$. The powder mixture is then ball-milled for 5 h in the high energy ball mill and finally uniaxially hot pressed for 8 min at 573 K under 85 MPa in a 12.7 mm graphite die.[27] The annealing temperature was chosen such that it remains far below the phase transition temperature to the detrimental and quite stable γ phase.

Thermoelectric Properties Characterization: Temperature-dependent Seebeck coefficient and electrical conductivity were measured using an in-house developed facility with a four-probe technique.[57,58] The measurement uncertainties for the Seebeck coefficient and the electrical conductivity are estimated at ± 5%. The weighted mobility, which is proportional to the thermoelectric quality factor B was calculated with the equation by Snyder et al.[59] $\mu_w = \frac{3h^3\sigma}{8\pi e(2m_e k_B T)^{3/2}} [\frac{\exp[\frac{|S|}{k_B/e}-2]}{1+\exp[-5(\frac{|S|}{k_B/e}-1)]} + \frac{\frac{3}{\pi^2}\frac{|S|}{k_B/e}}{1+\exp[5(\frac{|S|}{k_B/e}-1)]}]$ using our measured temperature dependent Seebeck coefficient and electrical conductivity. The thermal diffusivity (α) measurement was performed using a laser flash method (Netzsch LFA 427 apparatus) in argon atmosphere. From this, the thermal conductivity (κ) was calculated using $\kappa = \alpha\rho C_p$, where ρ and C_p are the sample density and heat capacity dependent on the composition at constant pressure, respectively. C_p was calculated using the Dulong-Petit limit estimating the specific heat at constant volume (c_V^{DP}) and a thermal expansion correction : $C_p = c_V^{DP} + \frac{9E_t^2 T}{\beta_T \rho}$, where E_t and β_T are the linear coefficient of thermal expansion and isothermal compressibility of MgAgSb respectively. The electronic thermal conductivity was estimated using the Wiedemann-Franz law by $\kappa_e = L\sigma T$ where L is the Lorenz number, calculated within a single parabolic band (SPB) model from the Fermi integrals $F_i(\eta)$ using $= (\frac{k_B}{e})^2 \frac{3F_0(\eta)F_2(\eta)-4F_1^2(\eta)}{F_0(\eta)^2}$. Due to the small band gap of MgAgSb, SPB is approximately only valid up to slightly above room temperature.[11] There the lattice contribution was then determined by subtracting κ_e from the total thermal conductivity $\kappa_{lat} = \kappa - \kappa_e$. Spatially resolved Seebeck coefficient maps at room temperature were obtained using an in-house developed transient Seebeck microprobe (TPSM) with a resolution of 3 to 5 µm[37,60] and a Potential & Seebeck Microprobe (PSM) with a resolution of 20 to 50 µm.[36] The technique involves positioning a sharp metallic microprobe on a sample's surface and applying a local temperature gradient across a small region of the sample. This gradient induces a voltage difference between the probe and the non-heated region of the sample, allowing for the determination of the Seebeck coefficient. A difference in temperature between the thermocouple junction and the point of thermovoltage measurement at the contact point of the probe can distort the temperature (difference) measurement, resulting in underestimated Seebeck coefficient values. This phenomenon is recognized as the cold finger effect and typically leads to reduction of 10 to 15% in the measured Seebeck value.[60]

Microstructural Characterization: Thin lamellae with a thickness of ≈100 nm were prepared by focused ion beam (FIB) using the FEI Helios NanoLab 600i Dualbeam microscope for some sintered pellets to further characterize their nanostructure performing STEM coupled with energy dispersive X-ray spectroscopy. A Philips Tecnai F30 equipped with a Super-Twin objective lens was used at an acceleration voltage of 300 keV. SAED patterns were captured using the Philips Tecnai F30 to identify the phases. The improved spatial resolution of STEM-EDS (lateral resolution of 10 nm) is ≈100 higher than that of SEM-EDS. STEM images where done using a HAADF detector. The background signal was calculated and removed. Finally, no deconvolution of the EDS spectra was done since no important overlapping of element peaks was observed. EDS point identification was also performed on the samples to identify the corresponding phases.

The overall effective composition of each sample was determined using the method described by Duparchy et al.[27] Essentially, SEM and EDS were utilized using a Hitachi High Tech's SU39000 SEM instrument. Numerous areas of ≈1 mm², each, were measured on each sample to obtain an average atomic composition. All measurements were calibrated using a virtually single-phase reference sample as outlined by Duparchy et al.[27]

Statistical Analysis: A statistical sensitivity analysis was conducted to provide insights into how the weighted mobility μ_w (as an output parameter), responds to changes in secondary phase content (input parameters). The goal is to quantify the impact of each phase on the mobility, using a statistical model, where phase effects are captured through both concentration-dependent and concentration-independent terms. The relationship between the mobility and the occurrence of secondary phases is discussed here inspired by classical composite models according to which effective transport quantities change linearly with small fractions of secondary phases[22–24] but also allows to capture further effects which are related to the bare fact of occurrence of a certain secondary phase, independently on its concentration, e.g. due to grain boundary decoration, grain boundary phases (complexions),[52,53,61] or by an interaction of the secondary phase with the point defect structure of the matrix phase. The analytical relation (ansatz) is given by

$$\mu_{w,j} = \mu_{\mathrm{w},0} + \sum_{i=1}^{n} \beta_i \cdot x_{i,j} + \sum_{i=1}^{n} f_i \cdot p_{i,j} \tag{1}$$

where the $x_i(j)$ represents the amount of the i-th phase in the j-th sample, β_i is the proportional sensitivity parameter for the i-th phase, $p_i(j)$ is the presence indicator for the phase i in sample j (1 if present, 0 otherwise), f_i is the mobility increment (lump shift) in case of presence of phase i and $\mu_{\mathrm{w},0}$ is the ideal weighted mobility in absence of any secondary phases. The equation will be employed analogously for the quality factor ($B = (\frac{k_\mathrm{B}}{e})^2 \ \frac{8\pi e(2m_\mathrm{e}k_\mathrm{B}T)^{3/2}}{3h^3} \ \frac{\mu_\mathrm{w}}{\kappa_\mathrm{L}} T$) and the temperature averaged figure of merit ($z\,T_\mathrm{avg} = \frac{1}{T_h - T_c} \ \int_{Tc}^{Th} zT(T)dT$ with $T_c = 300\ K$ and $T_h = 573\ K$)), where the average figure of merit zT_{avg} that an optimally doped material can achieve is proportional to the thermoelectric quality factor which itself is proportional to the material's weighted mobility divided by the thermal lattice conductivity $\frac{\mu_\mathrm{w}}{\kappa_\mathrm{L}}$.[62–64]

The objective is to determine $\mu_{w,\,0}$, β_i and f_i by minimizing the squared sum of the residuals: $\sum_j (r_j)^2 = \sum_j \mu_{\mathrm{exp},j} - \mu_{\mathrm{calc},j}$, where $\mu_{\mathrm{exp},\,j}$ is the experimentally determined weighted mobility and $\mu_{\mathrm{calc},\,j}$ the calculated value of the assumed model of linear superposition of the effects of individual secondary phases. A two-step iterative least squares fitting approach was employed to rapidly approach the multi-parameter solution: first, $\mu_{w,\,0}$ and the β_i values were fitted assuming $f_i = 0$ for all phases, and then the f_i were set free one by one while observing minimization of the sum of squared residuals in each iteration. During each iteration, outliers were identified and excluded based on a threshold of $2 \cdot \sigma$, where σ is the standard deviation of the residuals. This process ensures a balance between sensitivity and specificity, avoiding excessive exclusion of normal data while effectively identifying outliers. The iterative fitting continues until no further outliers were detected, leading to robust parameter estimates.

To evaluate the goodness of fit, the coefficient of determination (R^2) and the root-mean-square error (RMSE) were calculated. R^2 quantifies how well the experimental data is captured by the function and the parameters of the predicted mobility, explained by $R^2 = 1 - (\frac{\sum_\mathrm{res}}{\sum_{tot}})$, where $\sum_\mathrm{res} = \sum_j r_j^{\,2}$ is the sum of squared residuals, and $\sum_\mathrm{tot} = \sum_j (\mu_{\mathrm{exp},j} - \overline{\mu_\mathrm{exp}})^2$ is the total variability in the experimental (weighted) mobility. The RMSE provides the average magnitude of the residuals and is given by $R_\mathrm{r} = \sqrt{\frac{\sum_j r_j^{\,2}}{n}}$, with n the total number of samples. These metrics, alongside visual analysis of residuals and their distribution, confirmed the model's accuracy and reliability in describing the relationship between the secondary phases and the weighted mobility. The sensitivity study was conducted for $n = 35$ samples, to evaluate the effect of the secondary phases Mg_3Sb_2, Ag_3Sb, the silver-rich solid solution labelled (Ag), and Sb on the (effective) weighted mobility, quality factor and avergaed figure of merit of the MgAgSb samples.

Phase quantification has phase identification as requirement, which is not always feasible by easily available SEM-EDS and XRD. Therefore, in this work we have used STEM-EDS and SAED to determine the composition and the phase of the nm to µm-sized secondary phases, avoiding and clarifying ambiguities present in earlier works. Then, where possible, the content quantification of those phases by Rietveld refinement of the XRD diffractograms, which can be done with higher reliability if the phases are known. The XRD patterns were obtained using a Bruker D8 device with secondary monochromator, Co-Kα radiation (1.78897 Å) and a step size 0.01° in the 2θ range of 20–80°. Rietveld refinement was then conducted on each sample, fitting the peak patterns of the identified phases to obtain the weight percentage of each phase. The obtained data are displayed in Tables S1 and S2 (Supporting Information). The main difference between samples synthesized with and without cleaning step is that an Ag_3Sb nanophase forms when the jar is not cleaned. Such phase cannot be identified by XRD due to its low weight fraction (less than 5 wt.%) and the small particle size, hence it can't be quantified by Rietveld refinement. For a sensitivity analysis, a quantification of the nanophase content is required but was not possible here. Thus, the amount of nanophase cannot be used as an input parameter in the sensitivity analysis.

Supporting Information

Supporting Information is available from the Wiley Online Library or from the author.

Acknowledgements

The authors and the LUNA project team would like to acknowledge the government of North Rhine Westphalia for the funds received to finance the project. The author Amandine Duparchy would like to thank the German Academic Exchange Service (DAAD) for the financial support. The authors also would like to express their gratitude to Przemyslaw Blaschkewitz for his support with the TE measurements and Gregor Oppitz for the TPSM measurement.

Conflict of Interest

The authors declare no conflict of interest.

Data Availability Statement

The data that support the findings of this study are available from the corresponding author upon reasonable request.

Keywords

MgAgSb, microstructure, nanophase, sensitivity analysis, thermoelectric material, weighted mobility

Received: April 23, 2025
Revised: June 27, 2025

---

[1] N. Abas, A. Kalair, N. Khan, *Futures* **2015**, *69*, 31.
[2] A. Firth, B. Zhang, A. Yang, *Appl. Energy* **2019**, *235*, 1314.
[3] S. Twaha, J. Zhu, Y. Yan, B. Li, *Renewable Sustainable Energy Rev.* **2016**, *65*, 698.
[4] M. Zebarjadi, K. Esfarjani, M. S. Dresselhaus, Z. F. Ren, G. Chen, *Energy Environ. Sci.* **2012**, *5*, 5147.
[5] J. Yang, F. R. Stabler, *J. Electron. Mater.* **2009**, *38*, 1245.

[6] M. N. Hasan, M. Nafea, N. Nayan, M. S. Mohamed Ali, *Adv. Mater. Technol.* **2021**, *7*, 2101203.

[7] H. M. Elmoughni, A. K. Menon, R. M. W. Wolfe, S. K. Yee, *Adv. Mater. Technol.* **2019**, *4*, 1800708.

[8] R. C. O'Brien, R. M. Ambrosi, N. P. Bannister, S. D. Howe, H. V. Atkinson, *J. Nucl. Mater.* **2008**, *377*, 506.

[9] N. Jaziri, A. Boughamoura, J. Müller, B. Mezghani, F. Tounsi, M. Ismail, *Energy Rep.* **2020**, *6*, 264.

[10] G. J. Snyder, E. S. Toberer, *Nat. Mater.* **2008**, *7*, 105.

[11] Z. Liu, J. Mao, J. Sui, Z. Ren, *Energy Environ. Sci.* **2018**, *11*, 23.

[12] H. Zhao, J. Sui, Z. Tang, Y. Lan, Q. Jie, D. Kraemer, K. McEnaney, A. Guloy, G. Chen, Z. Ren, *Nano Energy* **2014**, *7*, 97.

[13] M. J. Kirkham, A. M. dos Santos, C. J. Rawn, E. Lara-Curzio, J. W. Sharp, A. J. Thompson, *Phys. Rev. B* **2012**, *85*, 144120.

[14] X. Meng, W. Cai, Z. Liu, J. Li, H. Geng, J. Sui, *Acta Mater.* **2015**, *98*, 405.

[15] L.-D. Zhao, G. Tan, S. Hao, J. He, Y. Pei, H. Chi, H. Wang, S. Gong, H. Xu, V. P. Dravid, C. Uher, G. J. Snyder, C. Wolverton, M. G. Kanatzidis, *Science* **2015**, *351*, 141.

[16] Y. Pei, X. Shi, A. LaLonde, H. Wang, L. Chen, G. J. Snyder, *Nature* **2011**, *473*, 66.

[17] R. Amatya, R. J. Ram, *J. Electron. Mater.* **2011**, *41*, 1011.

[18] P. Ying, R. He, J. Mao, Q. Zhang, H. Reith, J. Sui, Z. Ren, K. Nielsch, G. Schierning, *Nat. Commun.* **2021**, *12*, 1121.

[19] P. Ying, L. Wilkens, H. Reith, N. P. Rodriguez, X. Hong, Q. Lu, C. Hess, K. Nielsch, R. He, *Energy Environ. Sci.* **2022**, *15*, 2557.

[20] L. Y. Liangjun Xie, Y. Yu, G. Peng, S. Song, P. Ying, S. Cai, Y. Sun, W. Shi, H. Wu, N. Qu, F. Guo, W. Cai, H. Wu, Q. Zhang, K. Nielsch, Z. Ren, Z. Liu, J. Sui, *Science* **2024**, *382*, 8.

[21] A. Wieder, J. Camut, A. Duparchy, R. Deshpande, A. Cowley, E. Müller, J. de Boor, *Mater. Today Energy* **2023**, *38*, 101420.

[22] C. Gayner, Y. Amouyal, *Adv. Funct. Mater.* **2019**, *30*, 1901789.

[23] Y. Lin, M. Wood, K. Imasato, J. J. Kuo, D. Lam, A. N. Mortazavi, T. J. Slade, S. A. Hodge, K. Xi, M. G. Kanatzidis, D. R. Clarke, M. C. Hersam, G. J. Snyder, *Energy Environ. Sci.* **2020**, *13*, 4114.

[24] F. Garmroudi, I. Serhiienko, M. Parzer, S. Ghosh, P. Ziolkowski, G. Oppitz, H. D. Nguyen, C. Bourges, Y. Hattori, A. Riss, S. Steyrer, G. Rogl, P. Rogl, E. Schafler, N. Kawamoto, E. Muller, E. Bauer, J. de Boor, T. Mori, *Nat. Commun.* **2025**, *16*, 2976.

[25] I. Rodriguez-Barber, J. Camut, L. Luhmann, A. Cowley, E. Mueller, J. de Boor, *J. Alloys Compd.* **2021**, *860*, 158384.

[26] J. Camut, I. Barber Rodriguez, H. Kamila, A. Cowley, R. Sottong, E. Mueller, J. de Boor, *Materials* **2019**, *12*, 1857.

[27] A. Duparchy, L. Millerand, J. Camut, S. Tumminello, H. Kamila, R. Deshpande, A. Cowley, E. Mueller, J. de Boor, *J. Mater. Chem. A* **2022**, *10*, 21716.

[28] Z. Feng, J. Zhang, Y. Yan, G. Zhang, C. Wang, C. Peng, F. Ren, Y. Wang, Z. Cheng, *Sci. Rep.* **2017**, *7*, 2572.

[29] J. de Boor, T. Dasgupta, H. Kolb, C. Compere, K. Kelm, E. Mueller, *Acta Mater.* **2014**, *77*, 68.

[30] H. Kamila, A. Sankhla, M. Yasseri, N. P. Hoang, N. Farahi, E. Mueller, J. de Boor, *Mater. Today: Proc.* **2019**, *8*, 546.

[31] A. Sankhla, A. Patil, H. Kamila, M. Yasseri, N. Farahi, E. Mueller, J. de Boor, *ACS Appl. Energy Mater.* **2018**, *1*, 531.

[32] W. Petruk, L. J. Cabri, D. C. Harris, J. M. Sterwart, L. A. Clark, *Can. Mineral.* **1970**, *10*, 163.

[33] M. A. Peacock, L. G. Berry, *Geol. Series* **1940**, *44*, 47.

[34] E. Zintl, E. Husemann, *Aufbau der Materie* **1933**, *21*, 138.

[35] R. W. G. Wyckoff, *Crystal Structures*, 2nd ed. Interscience Publishers, New York, **1963**, *1*, pp. 7–83.

[36] K. H. Wu, C. I. Hung, P. Ziolkowski, D. Platzek, G. Karpinski, C. Stiewe, E. Mueller, *Rev. Sci. Instrum.* **2009**, *80*, 105104.

[37] S. Ghosh, H. Naithani, B. Ryu, G. Oppitz, E. Müller, J. de Boor, *Mater. Today Phys.* **2023**, *38*.

[38] F. Edler, K. Huang, *Meas. Sci. Technol.* **2020**, *41*, 22,

[39] Z. Liu, W. Gao, X. Meng, X. Li, J. Mao, Y. Wang, J. Shuai, W. Cai, Z. Ren, J. Sui, *Scr. Mater.* **2017**, *127*, 72.

[40] K. Toh, K. Suekuni, K. Hashikuni, H. Nishiate, U. Anazawa, C.-H. Lee, M. Ohtaki, *J. Mater. Sci.* **2022**, *57*, 11265.

[41] S. Y. Back, S. Meikle, T. Mori, *J. Mater. Sci. Technol.* **2025**, *227*, 57.

[42] Y. Zheng, C. Liu, L. Miao, H. Lin, J. Gao, X. Wang, J. Chen, S. Wu, X. Li, H. Cai, *RSC Adv.* **2018**, *8*, 35353.

[43] T. Zhang, B. Dong, X. Wang, *J. Mater. Sci.* **2021**, *56*, 13715.

[44] P.-J. Ying, *Chem. Mater.* **2015**, *27*, 909.

[45] T. Xiong, H. He, Y. Zhang, Y. Wu, C. Niu, M. Rong, *J. Mater. Sci.: Mater. Electron.* **2023**, *34*, 1632.

[46] H. Okamoto, *J. Phase Equilib. Diffus.* **2007**, *28*, 403.

[47] A. A. Nayeb-Hashemi, J. B. Clark, *Bull. Alloy Phase Diagrams* **1984**, *5*, 348.

[48] A. Jain, S. P. Ong, G. Hautier, W. Chen, W. D. Richards, S. Dacek, S. Cholia, D. Gunter, D. Skinner, G. Ceder, K. A. Persson, *APL Mater.* **2013**, *1*.

[49] J. E. Saal, S. Kirklin, M. Aykol, B. Meredig, C. Wolverton, *Jom* **2013**, *65*, 1501.

[50] J. de Boor, C. Compere, T. Dasgupta, C. Stiewe, H. Kolb, A. Schmitz, E. Mueller, *J. Mater. Sci.* **2014**, *49*, 3196.

[51] M. Wood, J. J. Kuo, K. Imasato, G. J. Snyder, *Adv. Mater.* **2019**, *31*, 1902337.

[52] R. Bueno Villoro, M. Wood, T. Luo, H. Bishara, L. Abdellaoui, D. Zavanelli, B. Gault, G. J. Snyder, C. Scheu, S. Zhang, *Acta Mater.* **2023**, *249*, 118816.

[53] R. Bueno Villoro, D. Zavanelli, C. Jung, D. A. Mattlat, R. Hatami Naderloo, N. Pérez, K. Nielsch, G. J. Snyder, C. Scheu, R. He, S. Zhang, *Adv. Energy Mater.* **2023**, *13*, 2204321.

[54] H. Naithani, E. Müller, J. d. Boor, in Proceedings of the The 41st International and 7th Asian Conference on Thermoelectrics (ICT/ACT 2025), Sendai, Japan, **2025**.

[55] Y. Liu, D. Z. Zhou, Y. Q. Li, A. J. Hong, J. H. Sui, J. M. Liu, Z. F. Ren, *J. Mater. Chem. A* **2018**, *6*, 2600.

[56] M. Yasseri, A. Sankhla, H. Kamila, R. Orenstein, D. Y. N. Truong, N. Farahi, J. de Boor, E. Mueller, *Acta Mater.* **2020**, *185*, 80.

[57] J. de Boor, C. Stiewe, P. Ziolkowski, T. Dasgupta, G. Karpinski, E. Lenz, F. Edler, E. Mueller, *J. Electron. Mater.* **2013**, *42*, 1711.

[58] J. de Boor, E. Muller, *Rev. Sci. Instrum.* **2013**, *84*, 065102.

[59] G. J. Snyder, A. H. Snyder, M. Wood, R. Gurunathan, B. H. Snyder, C. Niu, *Weighted Mobility. Adv. Mater.* **2020**, *32*, 2001537.

[60] P. Ziolkowski, G. Karpinski, T. Dasgupta, E. Müller, *Phys. Status Solidi* **2013**, *210*, 89.

[61] J. J. Kuo, S. D. Kang, K. Imasato, H. Tamaki, S. Ohno, T. Kanno, G. J. Snyder, *Energy Environ. Sci.* **2018**, *11*, 429.

[62] Y. Pei, H. Wang, G. J. Snyder, *Adv. Mater.* **2012**, *24*, 6125.

[63] A. Zevalkink, D. M. Smiadak, J. L. Blackburn, A. J. Ferguson, M. L. Chabinyc, O. Delaire, J. Wang, K. Kovnir, J. Martin, L. T. Schelhas, T. D. Sparks, S. D. Kang, M. T. Dylla, G. J. Snyder, B. R. Ortiz, E. S. Toberer, *Appl. Phys. Rev.* **2018**, *5*.

[64] S. D. Kang, G. J. Snyder, *arXiv:1710.06896 [cond-mat.mtrl-sci]* **2018**.